

Flow and heat transfer characterization for supercritical CO₂ during heat rejection

Pandey, Sandeep; Laurien, Eckart; Chu, Xu

In: 2nd European sCO₂ Conference 2018

This text is provided by DuEPublico, the central repository of the University Duisburg-Essen.

This version of the e-publication may differ from a potential published print or online version.

DOI: <https://doi.org/10.17185/duepublico/46079>

URN: <urn:nbn:de:hbz:464-20180827-124348-8>

Link: <https://duepublico.uni-duisburg-essen.de:443/servlets/DocumentServlet?id=46079>

License:



This work may be used under a [Creative Commons Namensnennung 4.0 International](https://creativecommons.org/licenses/by/4.0/) license.

FLOW AND HEAT TRANSFER CHARACTERIZATION FOR SUPERCRITICAL CO₂ DURING HEAT REJECTION

Sandeep Pandey*, Eckart Laurien

Institute of Nuclear Technology and Energy Systems
University of Stuttgart
Stuttgart, Germany

*Email: sandeep.pandey@ike.uni-stuttgart.de

Xu Chu

Institute of Aerospace Thermodynamics
University of Stuttgart
Stuttgart, Germany

ABSTRACT

Supercritical carbon dioxide (sCO₂) has a wide spectrum of application in different fields such as working fluid in energy production and conversion industries. Most of the applications employ sCO₂ in the near-critical region to gain maximum efficiency; however, it creates a problem in heat transfer prediction because of drastic change in thermophysical properties. Heat transfer to supercritical CO₂ gets affected by the buoyancy and thermal contraction during the heat rejection process in pre-cooler section of the power cycle based on recompression-Brayton power cycle. Thus, direct numerical simulations were conducted to simulate the cooling process in the near-critical region with a relatively moderate bulk Reynolds number of 5400 at two different heat fluxes. The simulation results show the impaired heat transfer during downward flow and an enhanced heat transfer during the upward flow, contrary to the heating of CO₂. In the downward flow, heat transfer is deteriorated initially but soon enough a heat transfer recovery was observed. The decomposition of skin friction factor and the Nusselt number was performed to understand the role of individual terms viz. laminar, turbulent and inhomogeneous contribution. The major contribution on skin friction factor was brought by the body force due to the gravity. While the turbulent and inhomogeneous part equally affects the Nusselt number in supercritical flows. The turbulence statistics such as Reynolds shear stress, turbulent kinetic energy, and turbulent heat flux typically shows an increasing trend for upward flow and decreasing trend for the downward flow. All these turbulence quantities show a recovery in downward flow case near to the outlet. To investigate this recovery, quadrant analysis was conducted to examine the role of sweep (Quadrant-4) and ejection (Quadrant-2) events. During the heat transfer deterioration, sweep and ejection events reduced greatly, this triggers the reduction in turbulence. The recovery in heat transfer is brought by the Quadrant-1 and 3 commonly known as outward and

wall-ward interaction events. After the recovery, these interaction events dominate the flow and it is completely opposite to the normal turbulence in which sweep and ejection events are significant. In addition to this, the turbulent heat flux in radial and streamwise direction became weaker along with a lesser number of frequencies during the buoyancy-favored flow. Turbulence anisotropy of Reynolds stress tensor is quantified by using the second and third invariants and it showed that the turbulence structure becomes rod-like during the deteriorated heat transfer regime in the downward flow.

INTRODUCTION

The lower critical pressure and temperature of carbon dioxide ($p_c=7.38$ MPa, $T_c=304.25$ K) as compared to water ($p_c=22.06$ MPa, $T_c=674.09$ K) provide an opportunity to generate power in the reduced operating range. The supercritical carbon dioxide (sCO₂) Brayton cycle takes the advantage of lower fluid density in the near-critical region to reduce the compression work and also circumvent the problem of dry-out, which occurs in sub-critical power cycles. There exist several plant layouts with carbon dioxide as the working fluid, including single and split flow layouts with the options of precompression, recuperation, intercooling, and reheating [1]. Among all these layouts, the recompression layouts have shown a great potential in terms of higher efficiency [2]. In a typical recompression Brayton cycle, isobaric heat addition takes place at high pressure as shown by process 2-3-4-5 in $T-s$ diagram in Figure 1, which is far away from the critical point (in the range of 20 to 25 MPa) and heat rejection takes place in the near-critical pressure (7.5 to 10 MPa) as depicted by process 6-7-8-1. The flow is split at Point 8, and the major part of the fluid is cooled down in the reject heat exchanger (i.e. pre-cooler) in process 8-1. The fluid is compressed isentropically in the compressor (process 1-2) and recompressor (process 8-3). During process 2-3, the major part of the split fluid is heated in the low-temperature recuperator and at point-3; it is mixed up

with the fluid coming from the recompressor. Then the fluid is sent to the high-temperature recuperator (process 3-4), where it extracts the heat from the fluid at the low-pressure side (process 6-7). The remaining part of the heat is supplied via an external source such as nuclear during the process 4-5. The isentropic expansion from high-pressure to low-pressure takes place in the turbine in process 5-6 and fluid is passed through the high and low-temperature recuperator for the regeneration purpose. The overall cycle promises high efficiency theoretically, yet might severely suffer from poor heat transfer termed as heat transfer deterioration, which arises in the near-critical region due to significant variation in the thermophysical properties.

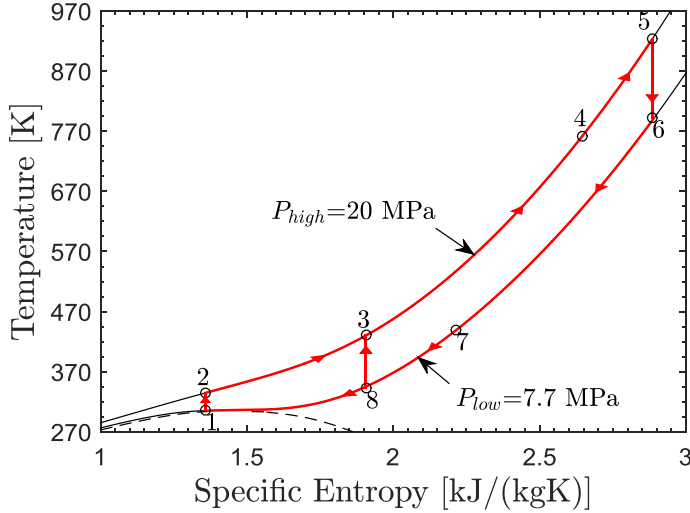


Figure 1: T-s diagram of the recompression Brayton cycle

At the high pressure of 20 MPa, thermophysical properties variation is smooth, thus commonly used correlation for constant properties can be applied to predict the heat transfer. The problem of an accurate and reliable prediction of heat transfer arises at the lower pressure, for e.g. at 7.7 MPa, where almost all thermophysical properties change abruptly. Heat transfer deterioration was observed in the near-critical region for heating of sCO₂ in various experiments, in which the wall temperature increased significantly due to poor heat transfer between the wall and bulk fluid [4]. Along with experiments, computational fluid dynamics (CFD) studies are an important tool which provides insight information. Numerous attempts have been made in the past to model the heat transfer to sCO₂ by means of turbulence modeling [5-7]. The turbulence models either over-predict or under-predict the heat transfer [5, 6]. Thus, direct numerical simulation (DNS) is an attractive alternative at low Reynolds numbers. Several DNS have been conducted specifically for CO₂ [8-10, 19]. Most of these DNSs were conducted for the heating of CO₂. Therefore, in this work, we made an attempt for DNS of cooling at different heat flux and direction of flow. We also examined few cases further by different turbulence techniques. The gained knowledge and DNS database can be used to develop analytical model or correlations [16-17]. The database also has a huge potential in machine learning based approach [18].

METHODOLOGY

In this DNS, the low-Mach Navier-Stokes (N-S) equations are used instead of the fully compressible N-S equations. This valid assumption was also employed by Bae et al. [8], Chu et al. [9, 11] and Nemati et al. [10]. Equations 1-3 represent the mass, momentum and energy conservation. In equations 1-3; ρ denotes the fluid density, u is the velocity vector, p is the pressure, μ represents the dynamic viscosity, h is the specific enthalpy, κ is the thermal conductivity and T denotes the temperature. The B_f is the body force due to gravity and its value is $[0, 0, \pm\rho g]^T$ and S represents the strain tensor.

$$\partial_t \rho + \nabla \cdot (\rho u) = 0 \quad (1)$$

$$\partial_t (\rho u) + \nabla \cdot (\rho u u) = -\nabla p + \nabla \cdot (2\mu S) \pm B_f \quad (2)$$

$$\partial_t (\rho h) + \nabla \cdot (\rho u h) = \nabla \cdot (\kappa \nabla T) \quad (3)$$

While solving the equations, all thermophysical properties are a function of enthalpy only. They are implemented by spline functions. These properties were derived from NIST REFPROP [3]. An open-source CFD code, OpenFOAM, has been used for this work. The code is overall second order accurate in both space and time.

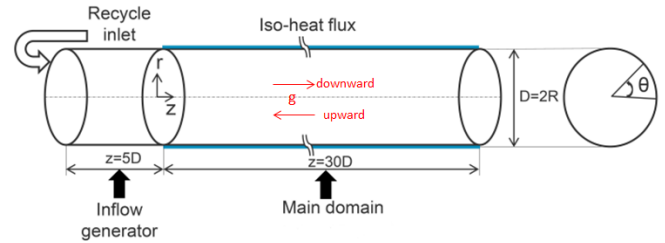


Figure 2: Computational domain

The simulation domain consists of a tube of 2 mm diameter with a total length of 35 diameters (35D) as depicted in Figure 2. The tube is divided into two parts: the inflow generator and the main domain. The inflow generator has a length of 5D. The objective of this section is to provide a fully developed turbulent flow to the main domain. For this purpose, a recycling procedure with the isothermal wall is adopted. A resolution of 120×360×300 was chosen for the inflow generator. The main domain is distinguished from the inflow generator by a uniform heat flux for the remaining length. In the main domain, the no-slip boundary condition is imposed on the wall and a convective outflow boundary condition is used for the velocity and other variables at the outlet. A resolution of 120×360×1800 was used in radial, circumferential and axial direction with structured hexahedral mesh for the main domain to resolve the small scales. Uniform grid spacing is used in the axial direction, while the radial grid is refined close to the wall. The non-dimensional grid resolution is given in wall units defined by $y^+ = y u_\tau / \nu_0$. Here, R is the radius of pipe, ν is the kinematic viscosity and u_τ is the friction velocity. The subscript ‘0’ is for the conditions corresponding to the inlet (i.e. $p_0 = 8$

MPa and $T_0 = 342.05$ K). The distinction between upward, downward and zero gravity (i.e. forced) flow are made by changing the body force term (B_f) in the streamwise momentum equation. This numerical procedure has been validated with the experiments as well as with the DNS (refer [9, 12]), therefore, no further validation is discussed here. Table 1 shows the simulation parameters for this study. Total six cases were simulated with the variation of body force and heat flux.

Table 1: Simulation parameters, inlet temperature= 342.05 K, inlet pressure= 8 MPa

Sr. No.	Case	B_f (kg/m ² s ²)	q_w (kW/m ²)	q_w/G (kW/kg-s)
1	FC8q1	0	-30.87	-0.57
2	UC8q1	$-\rho g$		
3	DC8q1	ρg		
4	FC8q2	0	-61.74	-1.14
5	UC8q2	$-\rho g$		
6	DC8q2	ρg		

RESULTS AND DISCUSSION

Direct numerical simulations have been accomplished with the conditions of Table 1 and various results are discussed in this section. Here, all quantities are averaged by either Reynolds averaging or Favre averaging depending upon the variable. After obtaining the mean quantity by either of the methods, further averaging was done in the circumferential direction. Turbulent statistics were obtained by averaging in time for at least 10 flow through times, corresponding to the 300-fold characteristic turbulent timescale. For the DNS, 400-1400, computational cores has been used where parallel efficiency was 80-110%. Approximately 150,000 cpu-hours are needed for 10 flow through time with 1400 cores.

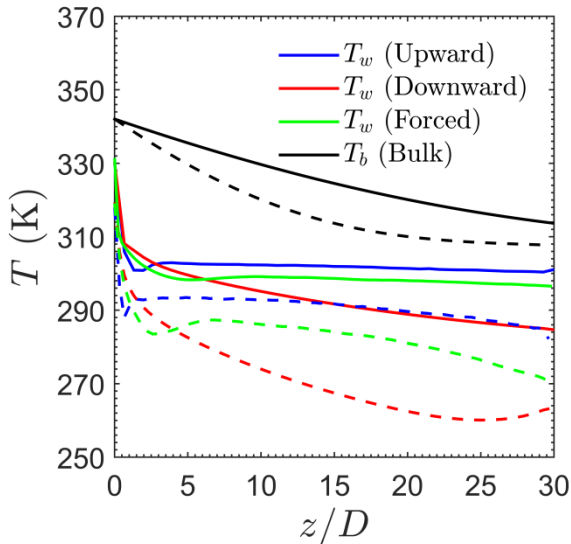


Figure 3: Variation of temperature along the axial direction; full lines: single heat flux (case 1-3); dashed lines: double heat flux (case 4-6)

Firstly, basic heat transfer characteristics are discussed. Figure 3 shows the variation of wall temperature for all six cases along with bulk temperature variation¹. The ' z/D ' represents the axial coordinates along the flow (i.e. streamwise) direction. The bulk enthalpy decreases linearly in the flow direction due to the negative uniform heat flux, and bulk temperature has a downward-concave profile due to the non-linear variation of the isobaric specific heat. Typically, the upward flow has the highest heat transfer coefficient indicated by the least difference between the bulk and wall temperature (see Figure 3), resulting in the highest Nusselt number. The flow with the downward direction suffers from the poor heat transfer. In the double heat flux case, a recovery can be observed near to the outlet. The density variation leads to a buoyancy effect, which gives rise to this dissimilar distribution of temperature in the forced and mixed convection. In upward flow cases, the wall temperature drops rapidly to the liquid-like region while the core fluid is still in the gas-like region. This sharp density gradient between the wall and core enhances the mixing of fluid radially, thereby promotes the heat transfer.

To analyze the hydraulic characteristics, skin friction factor ($C_f = \frac{2\tau_w}{\rho_b U_b^2}$) decomposition was performed, commonly known as FIK analysis [13-14]. We have re-derived this identity for supercritical carbon dioxide in this study. For the derivation, we first took the Favre-average of streamwise-momentum equation (i.e. Equation 3) and then integrate it two times. Following equation shows this relationship, the operator $\langle \rangle$ denotes fluctuations based on the cross-sectional area.

$$\begin{aligned}
 C_{f,FIK} = & -\frac{64}{\rho_b U_b^2 D^3} \int_0^R \underbrace{r \bar{\mu} \overline{S_{rz}}}_{C_1} r dr + \frac{64}{\rho_b U_b^2 D^3} \int_0^R \underbrace{r \overline{\rho u_r'' u_z''}}_{C_2} r dr \\
 & + \frac{32}{\rho_b U_b^2 D^3} \int_0^R (R^2 - r^2) \underbrace{\left\langle \frac{\partial \bar{p}}{\partial z} \right\rangle}_{C_3} r dr + \frac{64}{\rho_b U_b^2 D^3} \int_0^R \underbrace{r \bar{\rho} \tilde{u}_r \tilde{u}_z}_{C_4} r dr \\
 & + \frac{32}{\rho_b U_b^2 D^3} \int_0^R (R^2 - r^2) \underbrace{\left\langle \frac{\partial \bar{\rho} \tilde{u}_z \tilde{u}_z}{\partial z} \right\rangle}_{C_5} r dr + \frac{32}{\rho_b U_b^2 D^3} \int_0^R (R^2 - r^2) \underbrace{\left\langle \frac{\partial \bar{\rho} u_z'' u_z''}{\partial z} \right\rangle}_{C_6} r dr \\
 & - \frac{32}{\rho_b U_b^2 D^3} \int_0^R (R^2 - r^2) \underbrace{\left\langle \frac{1}{r} \frac{\partial r \mu' S_{rz}'}{\partial r} \right\rangle}_{C_7} r dr - \frac{32}{\rho_b U_b^2 D^3} \int_0^R (R^2 - r^2) \underbrace{\left\langle \frac{\partial \mu' S_{zz}'}{\partial z} \right\rangle}_{C_8} r dr \\
 & - \frac{32}{\rho_b U_b^2 D^3} \int_0^R (R^2 - r^2) \underbrace{\left\langle \frac{\partial \mu' S_{zz}'}{\partial z} \right\rangle}_{C_9} r dr \pm \frac{32}{\rho_b U_b^2 D^3} \int_0^R \underbrace{g(R^2 - r^2) \langle \bar{p} \rangle}_{C_{10}} r dr
 \end{aligned}$$

In this equation, $C_{f,FIK}$ is the skin friction factor computed by FIK identity using the above equation. In the equation, C_1 represents the laminar contribution, C_2 represents the turbulent contribution and C_{10} denotes the buoyancy contribution and '-' sign is for upward flow and '+' sign is for downward flow. Remaining quantities (C_3 - C_9) are for inhomogeneous contribution due to the variable properties. The quantity with overbar represents the Reynold averaged, with tilde shows the Favre averaged, with single prime represents the fluctuating part came out due to Reynolds averaging and double prime is the fluctuations based on Favre averaging. Figure 4 illustrates the implementation of this identity on Case UC8q2 and DC8q2.

¹ Corresponding DNS data are available at: <https://www.ike.uni-stuttgart.de/forschung/sco2/dns/>

The variation of C_1 , C_2 , C_4 , C_5 , and C_{10} can be seen; the remaining parts which are not shown here have negligible magnitude. The first observation is that the symbol ($C_{f,DNS}$) and line in black color ($C_{f,FIK}$) overlaps which suggests that accuracy of identity and its implementation on our cases. The downward flow case offers more hydraulic resistance to the fluid as compared to the upward flow. It is contributed by the buoyancy as shown later by means of term ' C_{10} '. In upward flow case, we observed a peculiarity in the skin friction factor (see Figure 4a). The value of C_f fluctuates around zero initially and then becomes negative. This is a result of the negative wall-normal gradient of streamwise velocity. It means that flow exhibits an annular type of flow in which the gradient in the near-wall region is negative but in the core region it turns to positive.

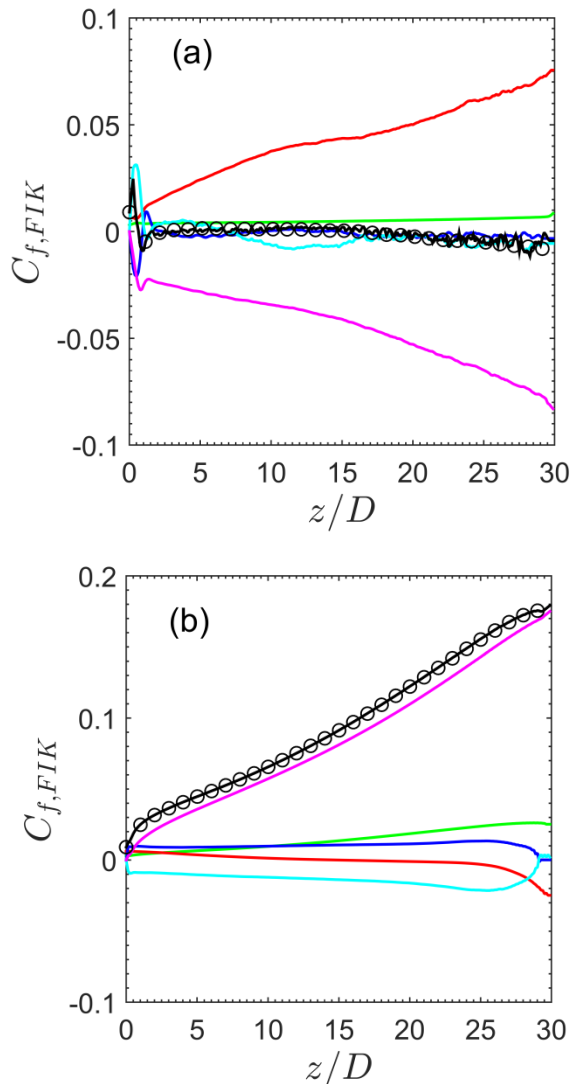


Figure 4: FIK analysis (a) Case UC8q2 and (b) DC8q2; green: C_1 , red: C_2 , blue: C_4 , cyan: C_5 , magenta: C_{10} , black: $C_{f,FIK}$, Symbols: C_f from DNS

In both the cases, the bulk Reynolds number decrease in the streamwise direction due to the cooling and it brings down the laminar contribution (C_1). The turbulent contribution (C_2) is decreasing due to the reduction in turbulent shear stress (not shown here). On the other hand, during the upward flow, turbulent shear stress increase and it contributes the comparatively higher magnitude of C_2 . The term C_4 depends on the mean velocity profiles in radial and axial directions as well as on the mean density. Their profiles remain approximately constant in the axial direction in case DC8; therefore, we observe an almost constant value in Figure 4b. A similar trend was observed for the upward flow except for a peak in the inlet region, in Figure 4a. The evolution of the streamwise momentum flux directly affects C_5 . Interestingly, the buoyancy contribution (C_{10}), has a notable contribution to the overall skin friction factor. For downward flow, C_{10} has a positive magnitude and is responsible for more than 90% of total hydraulic resistance (refer Figure 4b). The negative C_{10} is responsible for the very low skin friction in upward flow in Figure 4a. Though the decomposition of Nusselt number is not shown but a brief discussion is as follow. The results show a similar behavior i.e. enhanced heat transfer in upward flow is brought by the turbulent fraction while in downward flow turbulent contribution reduced significantly which caused ultimately the heat transfer deterioration. Through this analysis, one can deduce that upward flow should be preferred during the cooling of sCO₂ in heat exchangers as it will result in higher heat transfer rate and lower pressure drop due to the lesser hydraulic resistance.

A heat transfer recovery was observed earlier in case DC8q2 near to the outlet in Figure 3. To examine it, we perform conditional averaging of the Reynolds shear stress. This method is known as ‘‘Quadrant analysis’’ and for it, data of Reynolds shear stress were sampled based on the sign of $\sqrt{\rho}u_r''$ and $\sqrt{\rho}u_z''$. Depending on their sign, quadrants are named after the possible events which can take place. For instance, the first ($\sqrt{\rho}u_r'' > 0, \sqrt{\rho}u_z'' > 0$) and third ($\sqrt{\rho}u_r'' < 0, \sqrt{\rho}u_z'' < 0$) quadrant are known as the wall-normal and wall-ward interaction events, respectively. While the second ($\sqrt{\rho}u_r'' > 0, \sqrt{\rho}u_z'' < 0$) and the fourth ($\sqrt{\rho}u_r'' < 0, \sqrt{\rho}u_z'' > 0$) quadrants ($\sqrt{\rho}u_r'' < 0, \sqrt{\rho}u_z'' < 0$) are identified as ejection and sweep events, respectively. Ejection event indicates that low-streamwise velocity fluid is moving away from the wall with a high cross-stream velocity, and sweep event shows that high streamwise velocity fluid is moving towards the wall with a lower cross-stream velocity. (Here, high and low are with respect to the mean).

Figure 5 shows the analysis of downward flow case with double heat flux (i.e. case DC8q2) and these quadrants are normalized by the $\sqrt{\tau_w}$ at the inlet. The Quadrant-2 (ejection) and Quadrant-4 (sweep) have the major contribution to Reynolds shear stress at the inlet (at $z=0D$). At $z=15D$, all events suppress and this leads to the reduced turbulence in the flow. Ultimately, it will result in the deteriorated heat transfer in the downward flow. At $z=27.5D$, a growth in Quadrant-1 and 3

can be seen in Figure 5. This will recover the turbulence in the flow and results in the heat transfer recovery. An interesting point from this analysis is that heat transfer recovery is brought by the interaction events instead of the typical turbulence generation mechanism (ejection and sweep).

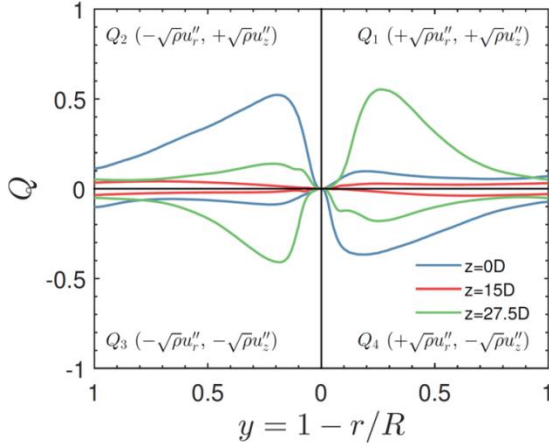


Figure 5: Quadrant analysis for Case DC8q2

The above-discussed quadrant analysis gives information regarding the time-averaged behavior of flow. To further analyze the heat transfer deterioration in the downward flow case (Case DC8q2), we investigate the frequencies of the events over time. We used a statistical technique known as weighted joint probability density function (JPDF), in which probabilities of events are multiplied by the corresponding magnitude. For this analysis, data were sampled at every 100th-time step for 10 flows through times. These data were sampled at different axial locations and here we discuss the few of them in the near-wall area. The iso-contours of weighted JPDF of radial turbulent heat flux is shown in Figure 6 for two different axial locations at r/R of 0.8 (corresponding $y^+=36$ based on inlet values). At $z=5D$, hot and cold wall-normal motions are responsible for the generation of turbulent heat flux in the wall normal direction. The contributions of existing quadrants become stronger downstream with increasing radial velocity.

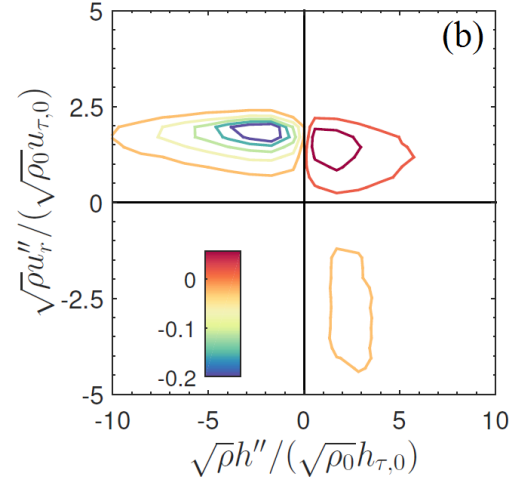
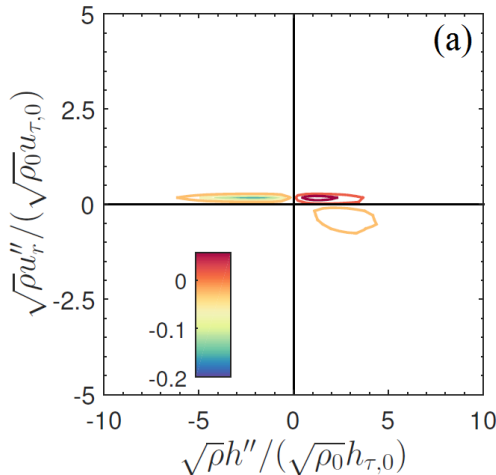


Figure 6: Iso-contours of weighted JPDF of radial turbulent heat flux for Case DC8q2; (a) $z=5D$ and (b) $z=27.5D$

Now, we provide a brief discussion on the role of anisotropy in the deteriorated downward flow case (Case DC8q2). This kind of analysis provides the information for properly predicting the amount and type of anisotropy, which is critical for accurate numerical simulation using the conventional modeling approach. The anisotropy is quantified by Reynolds stresses. The Reynolds stress is second order tensor (say b_{ij} , with $i,j=1,2,3$) in terms of a 3×3 matrix in which diagonal components are the normal stresses. Therefore, we remove the normal stress and only concentrate on the traceless part of this matrix (say b_{ij}'), and this is normalized by the turbulent kinetic energy. As a next step, the Eigenvalues (say λ_1 , λ_2 , and λ_3) of this normalized traceless matrix are calculated. Then two new variables are defined as; $\eta^2 = (\lambda_1^2 + \lambda_2^2 + \lambda_3^2)/3$ and $\xi^3 = -\lambda_1 \lambda_2 (\lambda_1 + \lambda_2)/2$. The degree of anisotropy is defined with the η and the characteristic shape described by the ξ . Figure 7a shows the mapping of η and ξ , the area bounded by the blue line is known as the Lumley triangle [15]. The vertex of this triangle at the origin is corresponding to the isotropic turbulence, the top right vertex is corresponding to the 1-dimensional turbulence and the left top vertex indicates the 2-dimensional axisymmetric turbulence. At the inlet, turbulence structure is 2-dimensional in near-wall region, while in the core region turbulence has prolate structure. Figure 7b shows the Lumley triangle for the deteriorated heat transfer at $z=15D$. We can see that turbulent structure become 1-component (or rod-like) in the near-wall while in the core region turbulence structure remains the same. This shift to 1-component turbulence structure indicates elongated streaks. The ejection events are responsible for breaking the streaks by ‘turbulent burst’ and allow the near-wall fluid to move away from the wall. But such events reduce greatly. This attenuates the near-wall turbulence and causes heat transfer deterioration. It suggests that modulation of near-wall turbulence leads to the poor heat transfer in the pipe.

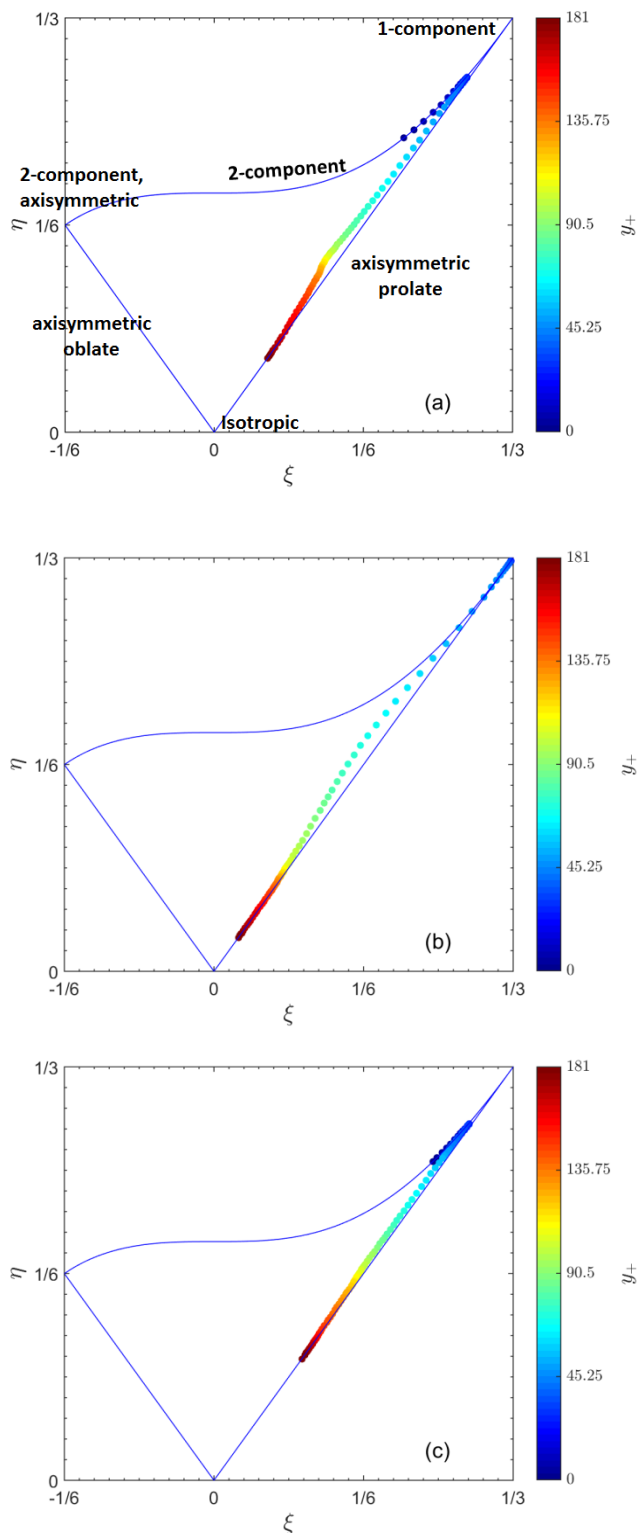


Figure 7: Lumely triangle to visualize the anisotropy of Reynolds stress tensor in the flow for Case DC8q2; (a) $z=0D$, (b) $z=15D$ and (c) $z=27.5D$

As soon as the heat transfer recovers at $z=27.5D$, a transition back to the 2-component can be observed in the

Figure 7c. As seen earlier in quadrant analysis, the recovery is brought by the interaction events. These interaction events promote the momentum transfer and result in recovery of turbulence thereby the increase in the heat transfer rate.

In the end, flow visualization is discussed with the help of low- and high-speed streak, and vortex. There are different ways by which one can identify the streaks in the flow. In this study, we used $\sqrt{\rho u_z''}$ to take density fluctuation into account. These streaks are identified as the low- and high-speed depending upon their signs and the term low and high correspond to the mean flow. The vortex structures are also identified with the help of λ_2 -criterion. The λ_2 is the second Eigenvalue of the symmetric tensor $s^2 + \omega^2$ with, s and ω as the symmetric and antisymmetric part of velocity gradient tensor. In this study, we use instantaneous velocity fields.

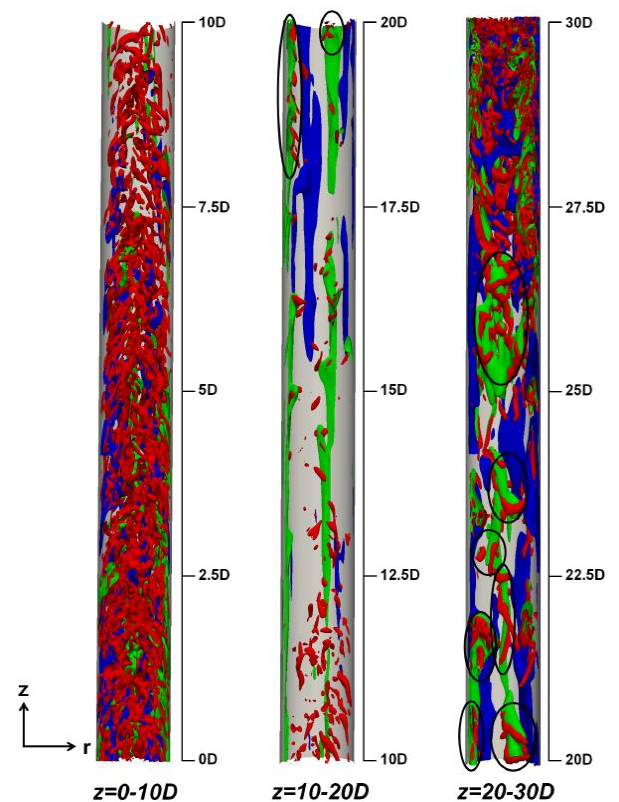


Figure 8: Iso-surfaces of streaks and vortex structure along the pipe for Case DC8q2; blue: low-speed streaks; green: high-speed streaks; red: λ_2 .

Figure 8 shows the iso-surfaces of low- and high-speed streaks along with the iso-surface of λ_2 to visualize the coherent turbulent structure. The λ_2 vortex starts reducing in the downstream direction and coherent structures start shifting away from the wall. The low-speed streaks are suppressed and strength of the coherent structure also reduced significantly. Moreover, high-speed streak survives in the flow of the deteriorated heat transfer regime and it is stretched out in the streamwise direction in the near-wall region as observed earlier.

After the reappearance of low-speed streaks at $z=15D$, λ_2 vortex also starts increasing and interestingly the coherent structures are superimposed mainly on the high-speed streak as highlighted with black circles.

SUMMARY

This study was motivated by the wide application of cooling of supercritical CO₂ especially in the pre-cooler section of the recompression-Brayton cycle. We carried out numerical experiments and these numerical experiments were conducted with an inlet temperature of 342.05 K and inlet pressure of 8 MPa, which are comparable with the reject heat exchanger in the proposed power cycle. Due to the computational limitations, a moderately low inlet Reynolds number was selected 5400. The results from 6 different DNS were presented here which include upward, downward flow along with the forced convection. The initial investigation shows heat transfer deterioration in downward flow and enhancement for the upward flow. The upward flow case shows a higher heat transfer rate and lower pressure drop due to the lesser hydraulic resistance, which promoted the upward flow orientation in the cooling. Further investigations were focused on the downward flow with double heat flux to understand the reason behind the heat transfer deterioration followed by recovery. We found out that sweep and ejection events which are responsible for the generation of turbulent stresses, decreased significantly and it triggers the attenuated heat transfer. In the deteriorated heat transfer regime, the streak elongates in the near-wall region and turbulence structure becomes rod-like. Near to the outlet section of the investigated domain, a heat transfer recovery was observed. The outward and wall-ward motions are responsible for this recovery, and it gives rise to the turbulent shear stress. In the recovery regime, we observed the streak breakdown and turbulence acquired 2-dimensional structure.

NOMENCLATURE

B_f	Body force ($\text{kg/m}^2\text{s}^2$)
C_1-C_{10}	Fractions of skin friction factor
C_f	Skin friction factor
D	Pipe diameter (m)
G	mass flux ($\text{kg/m}^2\text{-s}$)
h	Specific enthalpy (kJ/kg)
p	Pressure (Pa)
Q	Quadrant
r, θ, z	Radial, circumferential and axial coordinates
S	Strain rate (1/s)
s_s	Symmetric of velocity gradient tensor (1/s)
T	Temperature (K)
u	Velocity (m/s)
y	Distance from the wall (m)
κ	Thermal conductivity ($\text{W/m}^2\text{.K}$)
λ	Eigenvalue
μ	Dynamic viscosity (Pa-s)
ρ	Density (kg/m^3)
ω	antisymmetric part of velocity gradient tensor (1/s)

ACKNOWLEDGEMENTS

We are thankful to the *Forschungsinstitut für Kerntechnik und Energiewandlung (KE) e.V. Stuttgart*, and *High Performance Computing Center (HLRS) Stuttgart*.

REFERENCES

1. V. Dostal, M. Driscoll, P. Hejzlar, A supercritical carbon dioxide cycle for next generation nuclear reactors. Tech. rep. MIT (2004).
2. Y. Ahn, S.J. Bae, M. Kim, S.K. Cho, S. Baik, J.I. Lee, J.E. Cha, Review of supercritical CO₂ power cycle technology and current status of research and development, *Nucl. Eng. Technol.* 47 (6) (2015), 647–661.
3. E. Lemmon, M. Huber, M. McLinden, NIST standard reference database 23: reference fluid thermodynamic and transport properties-REFPROP, version 9.1 (2013).
4. H. Kim, Y. Bae, H. Kim, J. Soong, B. Cho, Experimental investigation on the heat transfer characteristics on a vertical upward flow of supercritical CO₂, in: *Proc. ICAPP, Reno, NV* (2006).
5. S. He, W. Kim, J. Bae, Assessment of performance of turbulence models in predicting supercritical pressure heat transfer in a vertical tube, *Int. J. Heat Mass Transfer* 51 (19–20) (2008), 4659–4675.
6. M. Sharabi, W. Ambrosini, S. He, J. Jackson, Prediction of turbulent convective heat transfer to a fluid at supercritical pressure in square and triangular channels, *Ann. Nucl. Energy* 35 (6) (2008), 993–1005.
7. A. Pucciarelli, I. Borroni, M. Sharabi, W. Ambrosini, Results of 4-equation turbulence models in the prediction of heat transfer to supercritical pressure fluids, *Nucl. Eng. Des.* 281 (2015), 5–14.
8. J.H. Bae, J.Y. Yoo, H. Choi, Direct numerical simulation of turbulent supercritical flows with heat transfer, *Phys. Fluids* 17 (10) (2005).
9. X. Chu, E. Laurien, Flow stratification of supercritical CO₂ in a heated horizontal pipe, *J. Supercrit. Fluids* 116 (2016), 172–189.
10. H. Nemat, A. Patel, B.J. Boersma, R. Pecnik, Mean statistics of a heated turbulent pipe flow at supercritical pressure, *Int. J. Heat Mass Transfer* 83 (2015), 741–752.
11. X. Chu, E. Laurien, D.M. McEligot, Direct numerical simulation of strongly heated air flow in a vertical pipe, *Int. J. Heat Mass Transfer* 101 (2016), 1163–1176.
12. X. Chu, E. Laurien, Direct numerical simulation of heated turbulent pipe flow at supercritical pressure, *J. Nucl. Eng. Radiat. Sci.* (2) (2016).

13. K. Fukagata, K. Iwamoto, and N. Kasagi, Contribution of Reynolds stress distribution to the skin friction in wall-bounded flows," *Physics of Fluids* 14 (2002).
14. H. Nemati, A. Patel, B. J. Boersma, and R. Pecnik, The effect of thermal boundary conditions on forced convection heat transfer to fluids at supercritical pressure," *Journal of Fluid Mechanics* 800 (2016), 531-556.
15. J. Lumley, and G. Newman, The return to isotropy of homogenous turbulence. *J. Fluid Mech.* 82 Lumley, J. & Newman, G. The return to isotropy of homogenous turbulence. *J. Fluid Mech.* 82 (1977), 161–178.
16. S. Pandey, E. Laurien, Heat transfer analysis at supercritical pressure using two layer theory, *J Supercritical Fluids* (2016), 80-86.
17. S. Pandey, E. Laurien, X. Chu, A modified convective heat transfer model for heated pipe flow of supercritical carbon dioxide, *Int. J. Therm. Sci.* 117 (2017), 227–238.
18. X. Chu, W. Chang, S. Pandey, J. Luo, B. Weigand, and E. Laurien, A computationally light data-driven approach for heat transfer and hydraulic characteristics modeling of supercritical fluids: From DNS to DNN, *Int. J. Heat Mass Transfer* 123 (2018), 629–636.
19. J. W. R. Peeters, R. Pecnik, M. Rohde, T. H. J. J. van der Hagen, and B. J. Boersma, Characteristics of turbulent heat transfer in an annulus at supercritical pressure, *Physical Review Fluids* 2 (2017), 024602.